

A Trailblazing Quenching Strategy for Simultaneous LiF Formation at Surface and Intergranular Interfaces for **Enhanced Stability of High-Ni NCM Cathodes**

Sung Joon Park, Hami Lee, Hee-Beom Lee, Hyunji Kweon, Bo Keun Park, Ji Won Kim, Fan Yun, Fang Zhang, Jongsoon Kim, * Young-Min Kim, * and Ki Jae Kim*

Water-washing effectively removes surface residual lithium from high-Ni LiNi_{0.8}Co_{0.1}Mn_{0.1}O₂ (NCM) cathodes; however, it inevitably degrades the electrochemical performance. To address this issue, integrated strategies targeting the conversion of surface residual lithium into artificial coating layers on high-Ni NCM cathodes have been proposed; however, these require further processing, thus hindering their industrial application. This study proposes a trailblazing strategy for directly converting residual lithium into a LiF layer simultaneously formed on both the surface of secondary particles and the interfaces between the primary particles of high-Ni NCM, without requiring further processing. This is achieved by modifying the conventional sintering process, with the main change being the replacement of the final air-cooling step with quenching, performed using a fluorinated ketone as a quenching medium. Furthermore, through controlled experiments conducted at various quenching temperatures, the distinct roles of surface and interfacial LiF in influencing the structural stability of high-Ni NCM cathodes are elucidated. Surface LiF primarily prevents electrolyte-induced side reactions, while interfacial LiF plays a crucial role in mitigating microcrack formation. Therefore, the full cell assembled using high-Ni NCM with surface and interfacial LiF layers and a graphite anode demonstrate a stable cycling performance over 300 cycles, highlighting the practical potential of this process.

1. Introduction

High-Ni LiNi_{0.8}Co_{0.1}Mn_{0.1}O₂ (NCM) cathode materials are the most preferred materials for meeting the demand for highenergy-density lithium-ion batteries (LIBs), owing to their high capacity and high average working voltage.[1-4] However, high-Ni NCM cathode materials suffer from severe capacity loss during charge/discharge, due to structural instability, irreversible phase transitions, oxygen evolution reactions, transition-metal dissolution, crack evolution, and electrolyte decomposition, which are accelerated by highly oxidative Ni⁴⁺ ions.^[5,6] Moreover, high-Ni NCM cathode materials easily react with ambient air and moisture, leading to the formation of residual lithium compounds, such as LiOH or Li₂CO₃, on their surfaces.^[7] These residual lithium compounds increase the difficulty of the manufacturing processes owing to the gelation of the cathode slurry, and they react with electrolytes to generate gas within LIBs,

S. J. Park, H. Lee, H.-B. Lee, H. Kweon, B. K. Park, J. Kim, Y.-M. Kim, Department of Energy Science

Sungkyunkwan University Suwon, Gyeonggi-do 16419, Republic of Korea

E-mail: jongsoonkim@skku.edu; youngmk@skku.edu; kijaekim@skku.edu

The ORCID identification number(s) for the author(s) of this article can be found under https://doi.org/10.1002/smll.202507292

© 2025 The Author(s). Small published by Wiley-VCH GmbH. This is an open access article under the terms of the Creative Commons Attribution-NonCommercial-NoDerivs License, which permits use and distribution in any medium, provided the original work is properly cited, the use is non-commercial and no modifications or adaptations are

DOI: 10.1002/smll.202507292

Thermo Fisher Scientific Hillsboro, OR 97124, USA J. W. Kim Department of Future Energy Engineering Sungkyunkwan University Suwon 16419, Republic of Korea F. Yun, F. Zhang NanoPort Thermo Fisher Scientific Pudong district, Shanghai, China, 201203 J. Kim, Y.-M. Kim, K. J. Kim SKKU Institute of Energy Science and Technology (SIEST) Sungkyunkwan University Suwon 16419 Republic of Korea Y.-M. Kim Center for 2D Quantum Heterostructures Institute for Basic Science (IBS) Suwon 16419, Republic of Korea

H.-B. Lee

Materials and Structural Analysis

www.advancedsciencenews.com



www.small-journal.com

which can cause serious safety concerns for LIBs.^[8] Thus, residual lithium compounds must be removed to meet the requirements for high-energy-density and long-lasting high-Ni NCM cathode materials.

In the field of cathode manufacturing, water-washing is commonly employed to remove residual lithium compounds from the surfaces of high-Ni NCM cathode materials.[9-11] Although this method effectively removes residual lithium compounds from the surfaces, it results in a slight decrease in discharge capacity owing to the unavoidable extraction of lattice Li.[12] In addition, water-washed samples exhibit increased sensitivity to H2O and CO2 in air, which limits the broader application of waterwashing.[13,14] To address these limitations of the water-washing process, various strategies have recently been proposed to convert surface residual lithium into organic or inorganic artificial coating layers on high-Ni NCM cathodes.[15-20] Specifically, LiFbased artificial coating layers have attracted considerable attention because of their electrochemical stability, weak adhesion to high-Ni NCM cathodes, prevention of excessive lattice distortion, and mitigation of microcrack formation. [21-25] Given the attractive features of LiF, numerous studies have used methods such as atomic layer deposition, solvothermal techniques, magnetron sputtering, and gas-phase reactions to synthesize LiF-coated high-Ni NCM cathodes (Table \$1, Supporting Information). [26–30] However, these methods still face challenges, such as the use of high-cost equipment, the requirement for further treatment, the use of toxic fluorinated gas, and the adoption of hard-to-handle substances. Furthermore, studies on the conversion of residual lithium on cathode surfaces into LiF have rarely been conducted because of the difficulties in both developing a methodology for forming a uniform LiF layer with selective reactions without the degradation of high-Ni NCM and achieving a controllable degree of reaction. Moreover, despite being frequently adopted, these strategies have not yet been adopted at the industrial manufacturing scale owing to the additional surface treatment required, which hinders productivity. Consequently, water-washing remains the standard in current manufacturing practices. Therefore, an innovative and scalable approach is required to enable the long-term use of high-Ni NCM cathode materials by overcoming the drawbacks of water-washing while maintaining process simplicity.

This study proposes an innovative surface reconstruction strategy that directly converts residual lithium compounds into LiF on both the surface of secondary particles and the interfaces between the primary particles of high-Ni NCM cathode materials. This surface reconstruction was achieved via simple modification of the conventional sintering process used for high-Ni NCM cathode materials, specifically by replacing the final air-cooling step in the current sintering process with quenching, performed using a fluorinated ketone as a quenching medium. Furthermore, by varying the quenching temperature in controlled experiments, we demonstrated the distinct roles of both the LiF formed on the surfaces of secondary particles and the LiF formed at the interfaces between primary particles in enhancing the structural stability of Ni-rich layered cathode materials. LiF formed on the surfaces of secondary particles mainly prevented electrolyte-induced side reactions, while LiF formed at the interfaces between primary particles played crucial roles in mitigating microcrack formation. Scheme 1 shows a schematic diagram of the modified sintering process, including the quenching step, as well as the anticipated roles of surface and interfacial LiF layers. Owing to the synergistic advantages of LiF layers on high-Ni NCM cathode materials, the full cell paired with a graphite anode achieved a stable cycling performance over 300 cycles, with an exceptionally ultralow capacity loss of 0.034% per cycle. This study represents a remarkable advancement in cathode engineering, providing a scalable and efficient strategy for practical applications in next-generation LIBs.

2. Results and Discussion

2.1. Surface Modification Using a Fluorinated Ketone

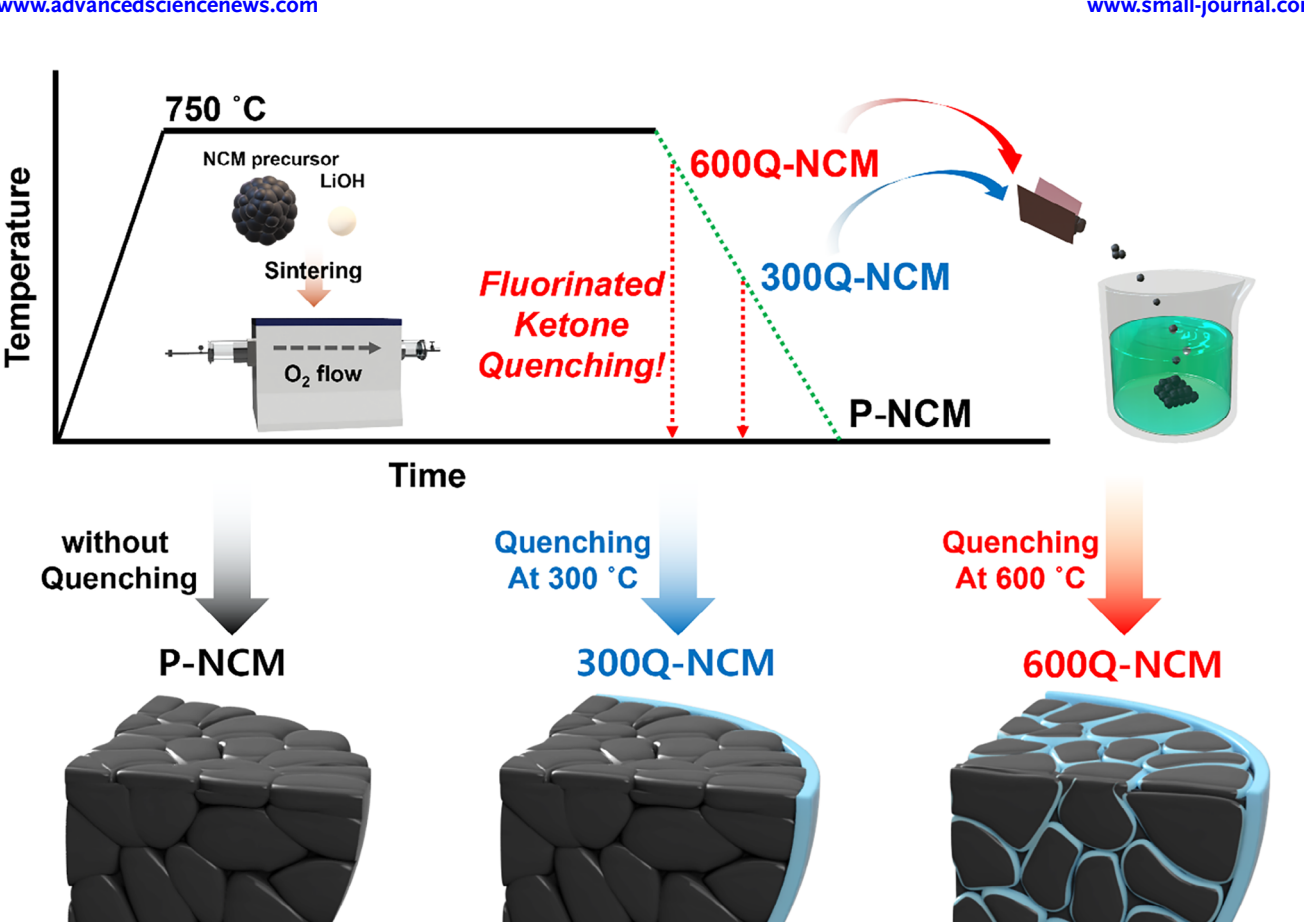
Our strategy for uniformly constructing a LiF layer on high-Ni NCM cathode materials fundamentally preserved the conventional sintering process without requiring additional treatment. The key modification was the replacement of the air-cooling step at the end of the sintering process with a quenching step, performed using a specialized quenching medium, that is, a fluorinated ketone. As shown in Equations (1) and (2), the fluorinated ketone reacted with residual lithium compounds (Li₂O), leading to LiF formation.

$$CF_3CF_2(C = O) CF(CF_3)_2 + \frac{1}{2}Li_2O \rightarrow CF_3CF_2(C = O) C(CF_3)_2 + LiF + \frac{1}{7}O_2$$
 (1)

$$CF_3CF_2(C = O) C(CF_3)_2 + \frac{1}{2}Li_2O \rightarrow CF_3CF(C = O) C(CF_3)_2 + LiF\frac{1}{4} + O_2$$
 (2)

To confirm the possibility of the occurrence of the suggested reactions, we performed first-principles calculations. The thermodynamic reaction pathways for LiF generation from the fluorinated ketone were calculated (Figure 1). The fluorinated ketone was ≈187 Hartree lower after defluorination, indicating that the defluorination of the fluorinated ketone for LiF formation was thermodynamically stable. The calculation indicates that, during quenching, the decomposition of the defluorinated product led to LiF formation, which was likely to form a LiF coating layer on the surface of NCM811. In addition, these reactions occurred at the liquid-solid interface between the residual lithium compounds and the fluorinated ketone. Consequently, depending on the quenching temperature, LiF was expected to form on the surfaces of secondary particles, at the interfaces between primary particles, or in both regions, owing to this unique reaction mechanism.

Before confirming the formation of LiF, verifying whether the introduction of the quenching process altered the structure and chemical composition of the high-Ni NCM cathode materials was necessary. Samples were prepared via quenching at 300 (denoted as 300Q-NCM) and 600 °C (denoted as 600Q-NCM), using a fluorinated ketone solvent after the sintering process. For comparison, a sample that underwent a conventional air-cooling step at the end of the sintering process was also



Primary particle protection

Medium residual lithium

Secondary particle protection

Scheme 1. Modified synthesis process for LiNi_{0.8}Co_{0.1}Mn_{0.1}O₂ cathode materials.

Primary particle protection

Rich residual lithium

Secondary particle protection

prepared (denoted as P-NCM). Focused Ga-ion beam scanning electron microscopy (FIB-SEM) and energy-dispersive X-ray spectroscopy (EDS) were used to analyze the physical and chemical changes in the cross-sectional structures of the primary and secondary particles following quenching.^[31] Figure 2a,b show the cross-sectional images and EDS mapping results for P-NCM, 300Q-NCM, and 600Q-NCM. Notably, all samples exhibited a cross-sectional structure typical of high-Ni NCM layered cathode materials, where secondary particles are composed of dense primary particles, and no discernible morphological differences were observed, even after quenching. Additionally, EDS maps of the major elements, namely Ni (orange), Mn (blue), Co (green), and O (red), revealed that all the elements were uniformly distributed throughout the secondary particles, with no elemental segregation or deficiency at either the inter- or intra-grain levels.

Moreover, the chemical compositions determined from energydispersive X-ray (EDS) maps (Table S2, Supporting Information) indicated that, at different quenching temperatures, the high-Ni NCM cathode materials did not affect the intrinsic chemical composition of the major elements. Furthermore, the calculated lattice parameters (a and c) and the c/3a ratios (Figure 2c,d; Note \$1, Supporting Information) were consistent across the samples, indicating that the overall crystal structure remained stable and unaffected by the proposed sintering process.[32,33]

To confirm the formation of LiF, its surface composition was further investigated using X-ray photoelectron spectroscopy (XPS). Figure 3a-i displays the C 1s, O 1s, and F 1s spectra of the surface chemical states of P-NCM, 300Q-NCM, and 600Q-NCM. P-NCM had no signal in the F 1s spectra, whereas 300Q-NCM and 600Q-NCM showed LiF compounds, observed at 685.0 eV,

Primary particle protection

Low residual lithium

Secondary particle protection

- Sungkyundavan University, Wiley Online Library on [24/10/20/25]. See the Terms and Conditions (https://onlinelblrary.wiley.com/terms-and-conditions) on Wiley Online Library for rules of use; OA articles are governed by the applicable Creative Commons License

www.small-journal.com

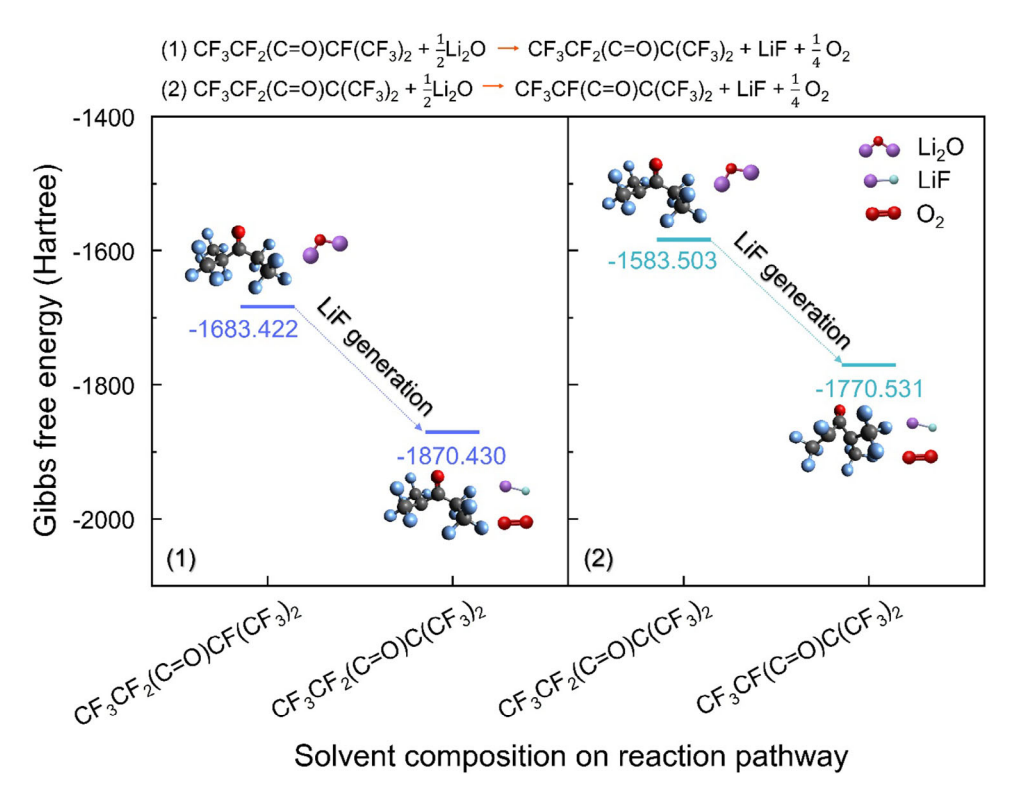


Figure 1. Comparison of the Gibbs free energy at each defluorination reaction state from a fluorinated ketone.

which arose from the reaction between the fluorinated ketone and residual lithium compounds.[34] As the reaction temperature increased, the intensity of the residual C-F peak (688.4 eV) decreased, indicating that the reaction became more vigorous at elevated temperatures.[35] Moreover, on the surface of 600Q-NCM, as residual lithium compounds were converted into LiF, the amount of Li₂CO₃ formed from the reaction between Li₂O and atmospheric CO₂ significantly decreased compared to that on the other sample surfaces, as summarized in Figure S1 (Supporting Information). This was further supported by the analysis of the NCM surface smoothness (Figure S2, Supporting Information) and residual lithium measurement results (Figure S3, Supporting Information) calculated using Equations S1 and S2 (Supporting Information). As the reaction temperature increased, the surface reactivity of NCM increased, resulting in more active reactions with the fluorinated ketone, converting residual lithium into LiF.

To further confirm whether LiF formed on the surface of the primary particles, at the interfaces between secondary particles, or in both regions, and to investigate how the LiF formation varied with quenching temperature, correlative microscopy combining FIB-SEM with time-of-flight secondary-ion mass spectrometry (TOF-SIMS) was employed. This multimodal approach allowed for the resolution of the elemental distribution of light elements (such as Li and F) in electrode materials over a cross-sectional sample from FIB-SEM imaging [36,37] Figure 4a shows representative cross-sectional images of the secondary particles of P-NCM, 300Q-NCM, and 600Q-NCM, which showed similar microstructures consisting of multiple primary particles. Figure

S4 (Supporting Information) shows TOF-SIMS normalized elemental distribution maps of F (19) and Li (7) for P-NCM, 300Q-NCM, and 600Q-NCM. The F distribution maps revealed that F ions unequivocally filled the surroundings of individual primary particles in the secondary particles of 300Q-NCM and 600Q-NCM, while F ion signals were not detected in P-NCM. Interestingly, in contrast to 300Q-NCM, F ions were strongly detected in the grain boundaries of 600Q-NCM, suggesting that, owing to the large temperature difference, the fluorinated ketone percolated along the grain boundaries of the high-Ni NCM cathode materials and subsequently reacted further with the residual lithium (Figure 4b). Based on the Li distribution maps, no distinctive differences were observed among P-NCM, 300Q-NCM, and 600Q-NCM, indicating that the consumption of Li for LiF formation was not due to Li in the lattice of the Ni-rich layered cathode materials but, rather, residual lithium present on the surface of the high-Ni NCM cathode materials. The observed different intensities of the Li ions in the primary grains and near the surfaces were attributed to topographical effects that altered the resulting secondary-ion signals, depending on both the presence of holes and the grain orientation.^[37,38] Based on the TOF-SIMS results, we confirmed that the quenching process conducted using fluorinated ketone could convert residual lithium compounds into an artificial LiF coating layer, while precise temperature control during quenching enabled the selective formation of LiF either on the surfaces of secondary particles or at the interfaces between primary particles. The additional HRTEM and EELS experiments confirmed the presence of LiF phase coating around the NCM primary particles (Figure S5, Supporting Information).

. 16136829, 2025, 42, Downloaded from https://onlinelibrary.wiley.com/doi/10.1002/smll.202507292 by Jongsoon Kim

Sungkyunkwan University, Wiley Online Library on [24/10/2025]. See the Terms and Conditions

onditions) on Wiley Online Library for rules of use; OA articles are governed by the applicable Creative Commons

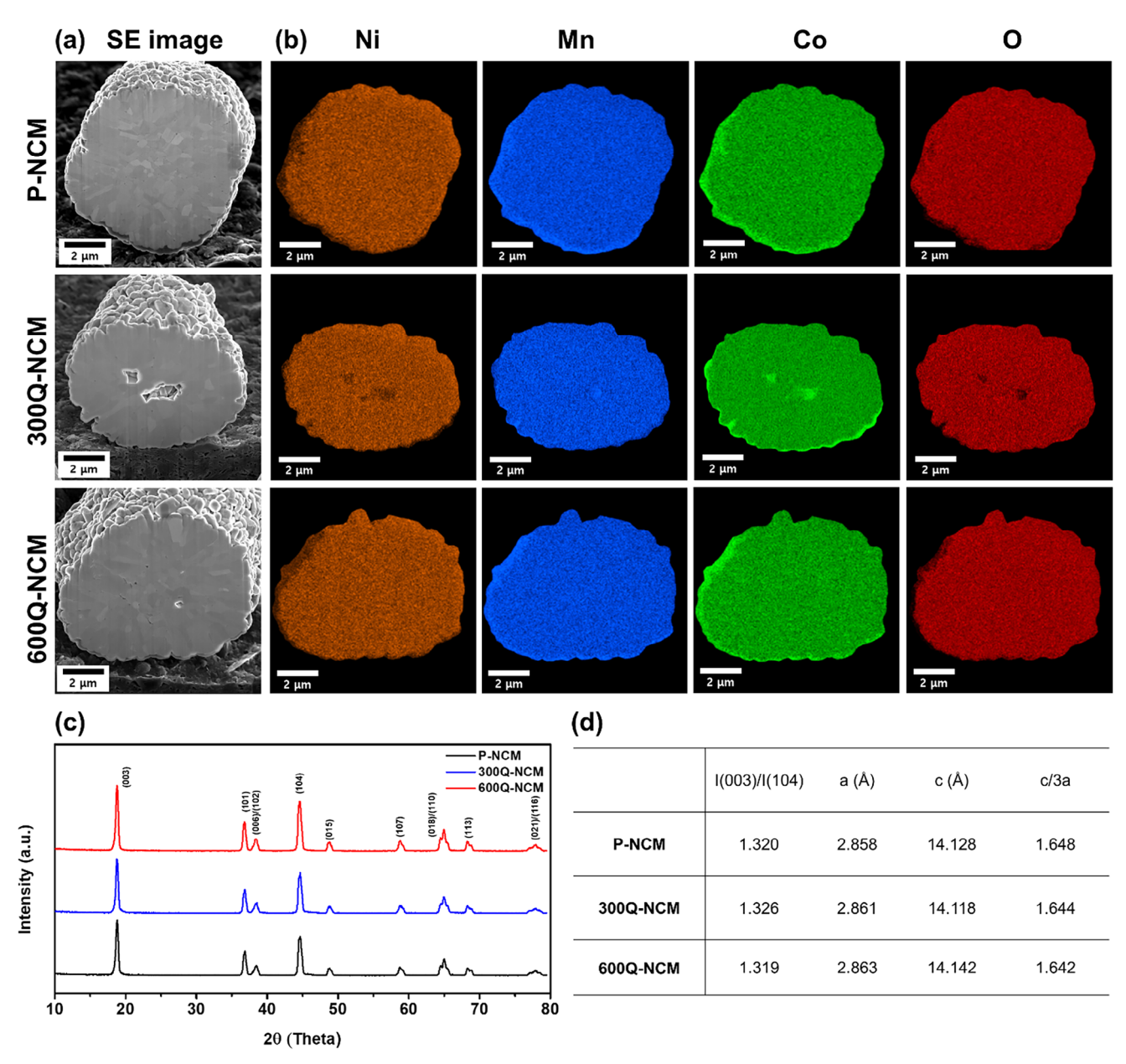


Figure 2. Elemental distribution maps of P-NCM, 300Q-NCM, and 600Q-NCM secondary particles at different annealing temperatures. a) SE images of cross-sectional samples prepared via FIB milling. b) EDX mapping results for the cross-sectional planes of secondary particles, which are displayed using false color codes: orange for Ni K (7.471 keV), blue for Mn K (5.894 keV), green for Co K (6.924 keV), and red for O K (0.525 keV). c) XRD results of P-NCM, 300Q-NCM, and 600Q-NCM, and d) corresponding lattice parameters.

2.2. Electrochemical Performance

To validate the effect of the LiF coating layer on the high-Ni NCM cathode materials, half-cells were fabricated using P-NCM, 300Q-NCM, and 600Q-NCM as cathodes. Cycling tests were performed at 1.0 C (1.0 C = 200 mA g^{-1}) and 30 °C within a voltage range from 2.8 to 4.3 V (vs Li/Li+). As shown in Figure S6 (Supporting Information), the 600Q-NCM exhibited the highest capacity retention of 89.6% over 100 charge-discharge cycles, compared to those of the other samples (P-NCM: 83.3%, 300Q-NCM: 87.4%). Moreover, even at a high cutoff voltage of 4.5 V (vs Li/Li⁺),

600Q-NCM showed the highest discharge capacity of 159 mA h g^{-1} after 100 cycles (P-NCM: 143 mA h g^{-1} , 300Q-NCM: 146 mA h g⁻¹), (**Figure 5**a; Figure S7, Supporting Information). In addition, even at a high current density of 8.0 C (Figure 5b; Figure S8, Supporting Information), 600Q-NCM exhibited the highest capacity of 81 mA h g^{-1} , outperforming both P-NCM and 300Q-NCM (7 mA h $\rm g^{-1}$ and 58 mA h $\rm g^{-1}$ for P-NCM and 300Q-NCM, respectively). The superior rate capability of 600Q-NCM was likely due to enhanced Li⁺ diffusivity and a reduced charge transfer resistance, as confirmed by the results of galvanostatic intermittent titration technique measurements and electrochemical

16136829, 2025, 42, Downloaded from https://onlinelibrary.wiley.com/doi/10.1002/smll.202507292 by Jongsoon Kim - Sungkyunkwan University , Wiley Online Library on [24/10/2025]. See the Terms and Conditions

conditions) on Wiley Online Library for rules of use; OA articles are governed by the applicable Creative Commons License



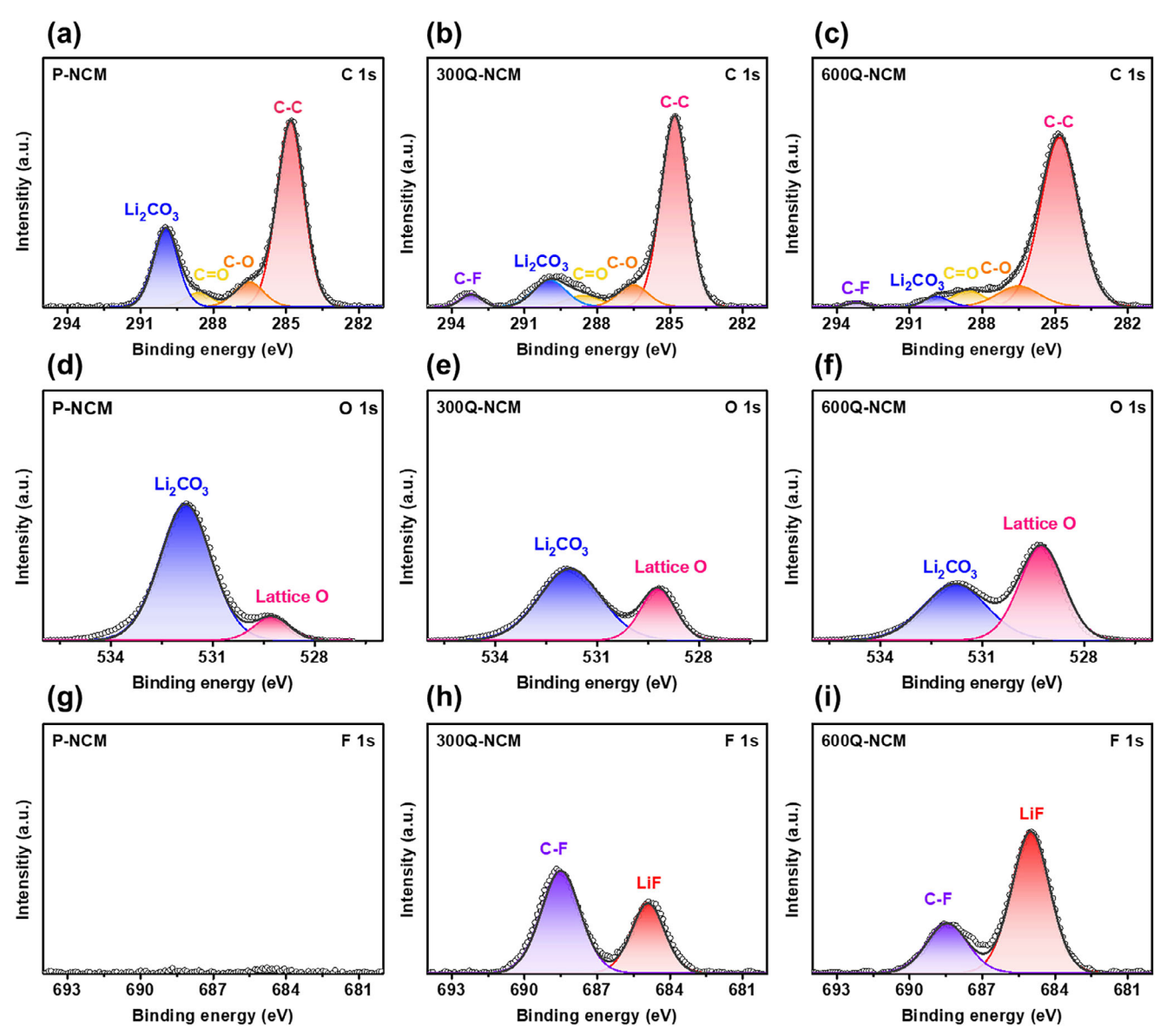


Figure 3. a-c) C 1s, d-f) O 1s, and g-i) F 1s results of P-NCM, 300Q-NCM, and 600Q-NCM.

impedance spectroscopy (Figures S9 and S10, Supporting Information). Given that LiF is known to act as both a protective layer that prevents side reactions at electrolyte–cathode interfaces and a Li-ion conductive layer, it was concluded that the improved cycling and rate performances of 600Q-NCM were mainly due to the uniformly formed LiF protective layer fully covering both the surface of secondary particles and the interfaces between primary particles, which made it much more effective in preventing side reactions at electrolyte–cathode interfaces than the LiF protective layer formed only on the surfaces of secondary particles.

Owing to the positive effects of the LiF formed on both the secondary particles and the interfaces between the primary particles, the full cell assembled with 600Q-NCM and a commercial graphite anode exhibited an enhanced cycling performance under standard conditions (Figure S11, Supporting Information).

Notably, even under more severe working conditions with a high cut-off voltage of 4.4 V, the full cell equipped with 600Q-NCM offered superior electrochemical stability, as shown in Figure 5c and Figure S12 (Supporting Information). To understand the superior electrochemical performance of 600Q-NCM, differential capacity (dQ/dV) curves, which provide information regarding the phase transitions during repeated charge/discharge processes, were compared in Figure 5f-g. The phase transition of the NCM811 cathode materials generally begins with a transformation from the hexagonal H1 phase to the monoclinic M phase, followed by a transition to the hexagonal H2 phase and finally to the hexagonal H3 phase. Within the coexisting two-phase regions, the transition potentials were ≈ 3.7 , 3.9, and 4.2 V for the H1-M, M-H2, and H2-H3 transitions, respectively. The H2→H3 phase transition was characterized by an abrupt contraction along the c-axis, leading to significant anisotropic lattice volume changes,

16136829, 2025, 42, Downloaded from https://onlinelibrary.wiley.com/doi/10.1002/smll.202507292 by Jongsoon Kim - Sungkyunkwan University , Wiley Online Library on [24/10/2025]. See the Terms and Conditions (https://onlinelibrary.wiley.com/doi/10.1002/smll.202507292 by Jongsoon Kim - Sungkyunkwan University , Wiley Online Library on [24/10/2025]. See the Terms and Conditions (https://onlinelibrary.wiley.com/doi/10.1002/smll.202507292 by Jongsoon Kim - Sungkyunkwan University , Wiley Online Library on [24/10/2025]. See the Terms and Conditions (https://onlinelibrary.wiley.com/doi/10.1002/smll.202507292 by Jongsoon Kim - Sungkyunkwan University , Wiley Online Library on [24/10/2025]. See the Terms and Conditions (https://onlinelibrary.wiley.com/doi/10.1002/smll.202507292 by Jongsoon Kim - Sungkyunkwan University , Wiley Online Library on [24/10/2025]. See the Terms and Conditions (https://onlinelibrary.wiley.com/doi/10.1002/smll.202507292 by Jongsoon Kim - Sungkyunkwan University , Wiley Online Library on [24/10/2025]. See the Terms and Conditions (https://onlinelibrary.wiley.com/doi/10.1002/smll.202507292 by Jongsoon Kim - Sungkyunkwan University , Wiley Online Library on [24/10/2025]. See the Terms and Conditions (https://onlinelibrary.wiley.com/doi/10.1002/smll.202507292 by Jongsoon Kim - Sungkyunkwan University , Wiley Online Library on [24/10/2025]. See the Terms and Conditions (https://onlinelibrary.wiley.com/doi/10.1002/smll.2025072).

and-conditions) on Wiley Online Library for rules of use; OA articles are governed by the applicable Creative Commons License

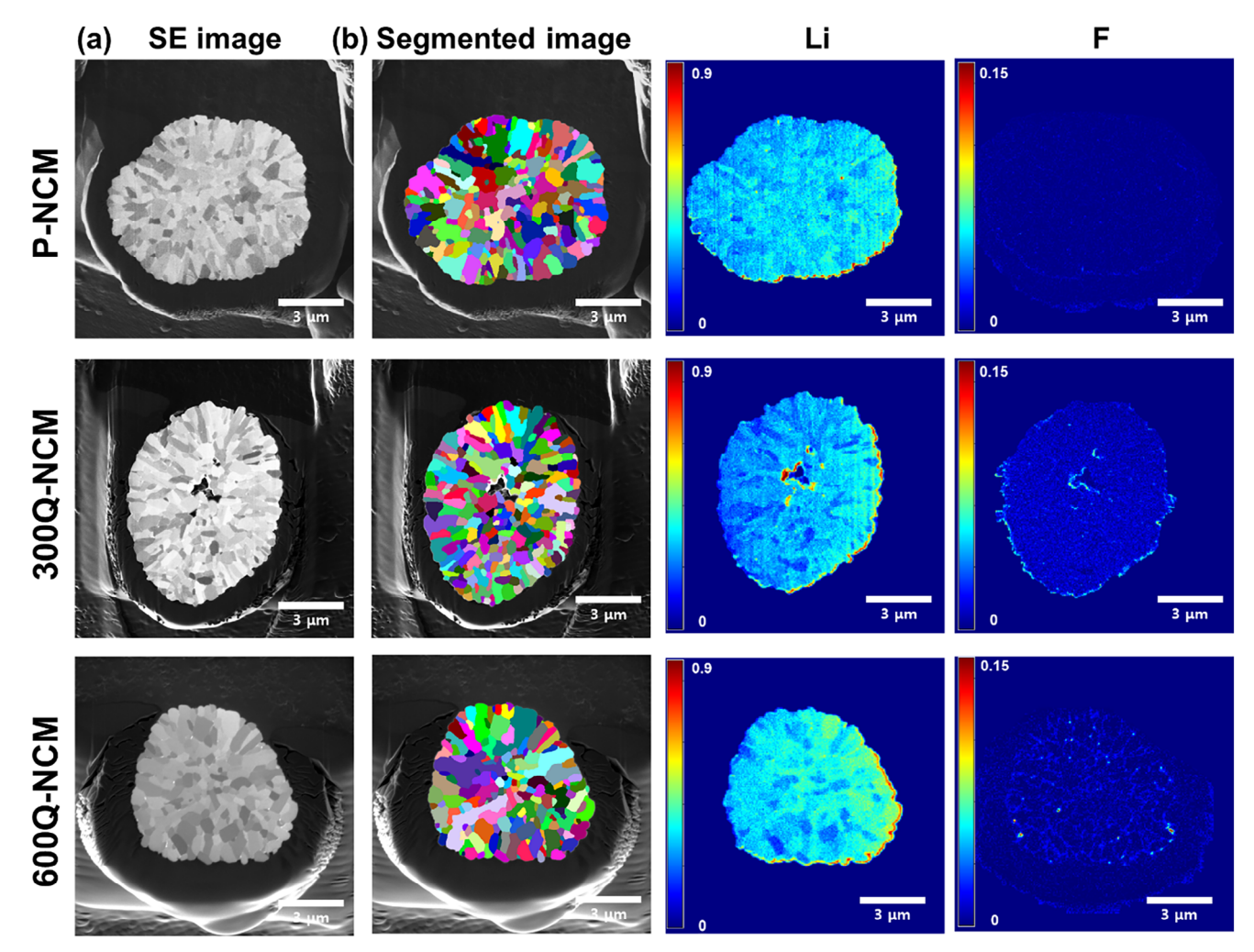


Figure 4. FIB-SEM/TOF-SIMS mapping for pristine NCM and LiF-treated NCM secondary particles. a) Cross-sectional FIB-SEM SE images of samples. b) (top) False-color-coded segmentation maps of primary particles in the four samples and (bottom) histograms of primary-particle size distributions calculated from these segmentation maps. Of note, the primary-particle diameter was calculated from the segmented area of a primary particle by assuming a circular particle shape.

which ultimately contributed to particle fracture and mechanical degradation. [39,40] Based on these general backgrounds, the dO/dV analysis revealed that 600Q-NCM exhibited the most stable phase transitions throughout repeated charge/discharge cycles. Contrastingly, the P-NCM cathode showed significant phase changes, suggesting structural instability and progressive degradation over time. Finally, the efficacy of the LiF coating layer of the Ni-rich layered cathode materials was evaluated in terms of the electrochemical performance under high-temperature conditions (Figure 5d; Figure S13, Supporting Information). The initial capacity of 163 mA h g-1 in the full cell equipped with P-NCM decreased to 114 mA h g⁻¹ over 100 cycles. However, 600Q-NCM delivered a substantially higher capacity (initial capacity: 172 mA h g⁻¹, after 100 cycles: 131 mA h g⁻¹). Consequently, the uniformly formed LiF on both the secondary particles and the interfaces between the primary particles played a critical role in suppressing irreversible phase transformations and minimizing electrode degradation induced by side reactions. This, in turn, enhanced the cycling stability and enabled the reliable operation of lithium-ion batteries under severe operating conditions, including high-temperature and high-voltage conditions.

2.3. Post-Mortem Analysis

To further confirm that the uniformly formed LiF on both the primary particles and the interfaces between the secondary particles was considerably more effective in protecting the NCM cathode materials against structural degradation, which was electrochemically demonstrated in the previous section, the cycled P-NCM, 300Q-NCM, and 600Q-NCM cathodes were analyzed using a transmission electron microscope. For P-NCM (Figure 6a), the surface was evidently covered by a thick rock-salt structure, while the bulk exhibited layered structures, indicating significant surface phase transformation during cycling. In contrast, 300Q-NCM, which had LiF only on the secondary particles, exhibited a relatively thin rock-salt structure compared to that of P-NCM (Figure 6b). Notably, for 600Q-NCM, only a negligibly disordered

16136829, 2023, 42, Downloaded from https://onlinelibrary.wiley.com/doi/10.1002/snll.2025/79292 by Jongsoon Kim - Sungkyunkwan University , Wiley Online Library on [24/10/2025]. See the Terms and Conditions (https://onlinelibrary.wiley.com/retrns-

and-conditions) on Wiley Online Library for rules of use; OA articles are governed by the applicable Creative Commons License

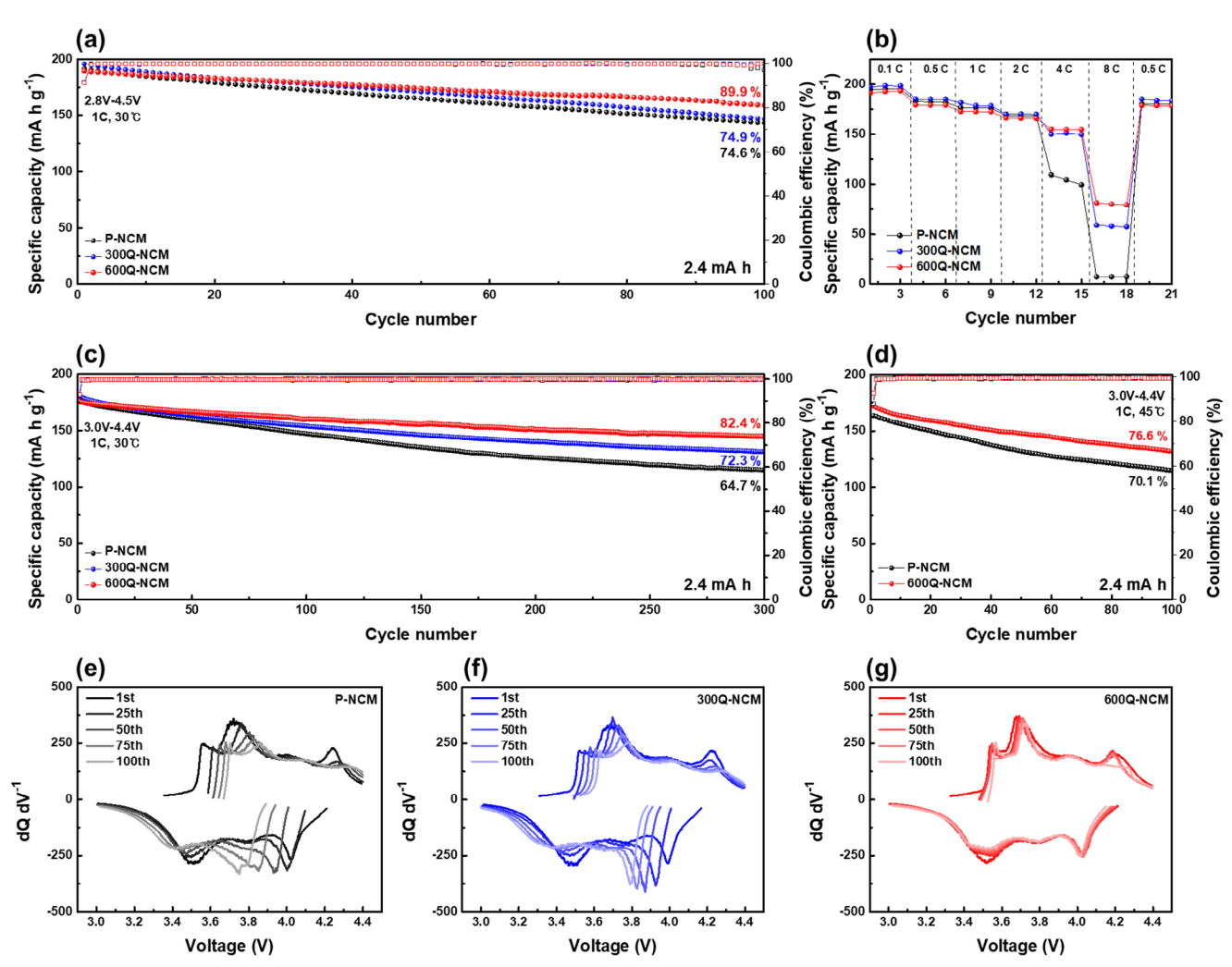


Figure 5. a) Cycling performance of half-cells with a high cut-off voltage of 4.5 V (vs Li/Li^+). b) Rate capability of various cathode materials. c) Cycling performance of a full cell with a working voltage range of 3.0–4.2 V. d) Cycling performance with increasing temperature and at high cut-off voltages e–g) dQ/dV curves derived from a full cell with a high cut-off voltage, for various cathode materials.

rock-salt layer was observed on the outer surface, while its layered structure remained intact (Figure 6c). [41–43] XPS analysis was conducted to further evaluate how LiF coating layers affect the growth of CEI layers resulting from continuous side reactions between a cathode and an electrolyte. In the Ni 2p spectra, the intensity of NiF2 and NiO, which are resistance-increasing residues formed by side reactions during 100 cycles, was the lowest for 600Q-NCM (Figure 6d-f). [44,45] Furthermore, in the F 1s spectra, the intensity of the Li_vPO_vF_z component, which indicated lithium salt (LiPF₆) decomposition due to its strong oxidizing property in the high-voltage range, was also the lowest for 600Q-NCM (Figure 6g-i; Figure S14, Supporting Information).[46] Based on structural and compositional post-mortem analyses, we suggest that the main role of the LiF layer on secondary particles was to prevent direct contact between the electrolyte and the highly reactive cathode surface, which would suppress the formation of the impedance-increasing disordered rock-salt phase and mitigate the accumulation of residues on the cathode surface during cycling.

During cycling, repetitive lithiation and de-lithiation within NCM led to changes in the particle volume and the formation of microcracks between the primary particles, which, in turn, allowed electrolyte penetration into these microcracks, ultimately resulting in long-term performance degradation. The formation of microcracks strongly depended on the interface structure between the primary particles. Therefore, the structural stability of interfaces could be reinforced by LiF formation, which enhances resistance against microcrack formation. To confirm this, cross-sectional images of P-NCM, 300Q-NCM, and 600Q-NCM were analyzed before and after cycling tests. Before cycling, none of the samples showed microcracks at the interfaces between primary particles (Figure S15, Supporting Information). However, after 100 cycles, significant differences became apparent. For P-NCM (Figure 7a), numerous microcracks propagated extensively along the interfaces between primary particles, resulting in the complete collapse of secondary particles. In contrast, for 300Q-NCM (Figure 7b), although microcracks also formed along the interfaces between

16136829, 2025, 42, Downloaded from https://onlinelibrary.wiley.com/doi/10.1002/smll.202507292 by Jongsoon Kim - Sungkyunkwan University, Wiley Online Library on [24/10/2025]. See the Terms and Online Company of the Company of the

on Wiley Online Library for rules of use; OA articles are governed by the applicable Creative Commons

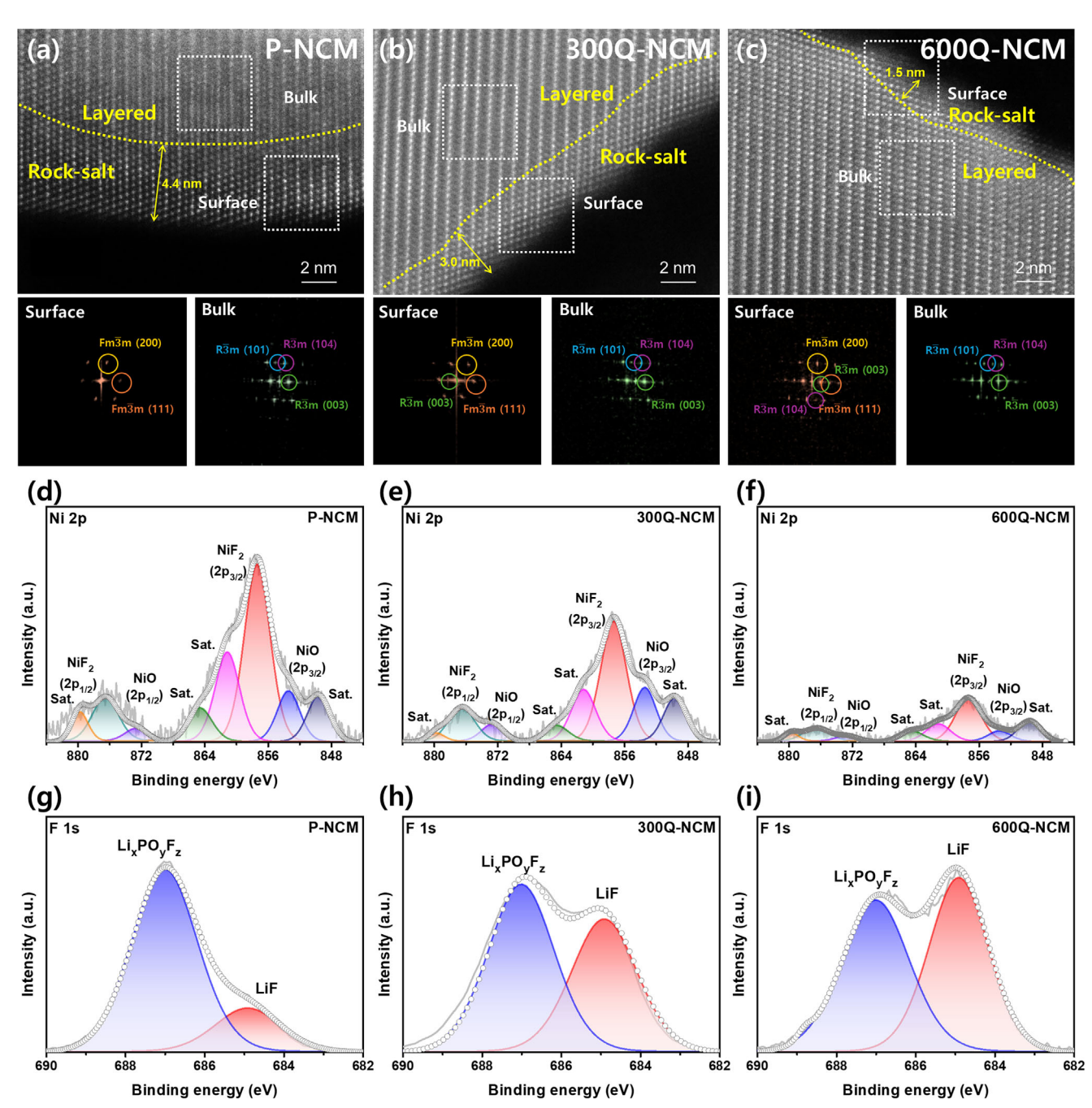


Figure 6. STEM images of a) P-NCM, b) 300Q-NCM, and c) 600Q-NCM cathode materials after 100 cycles, and the corresponding FFT patterns. XPS results after 100 cycles for d-f) Ni 2p and g-i) F 1s spectra of P-NCM, 300Q-NCM, and 600Q-NCM, respectively.

the primary particles, the extent of damage was moderately lower than that of P-NCM, indicating that the LiF formed on the surfaces of the secondary particles moderately inhibited microcrack formation. Notably, in the case of 600Q-NCM, only a negligible amount of microcracks was observed, suggesting that the structural stability of the interfaces between the primary particles could be reinforced by LiF formation (Figure 7c). Ultimately, the interface reinforcement induced by LiF formation at the interfaces between the primary particles enhanced the resistance to microcrack formation over prolonged cycling, leading to a superior electrochemical performance for 600Q-NCM. It is well-known that, as the number of microcracks increases in NCM cathodes, a large amount of transition-metal ions dissolve into the electrolyte, followed by their deposition onto the surface of the graphite anode, thereby degrading the electrochemical performance of the graphite anode. Therefore, further evidence of an improved interfacial and structural stability of the NCM cathodes can be obtained by measuring the extent of transition-metal dissolution. Inductively coupled plasma-mass spectrometry was used to measure the degree of transition-

and-conditions) on Wiley Online Library for rules of use; OA articles are governed by the applicable Creative Commons

www.advancedsciencenews.com

www.small-journal.com

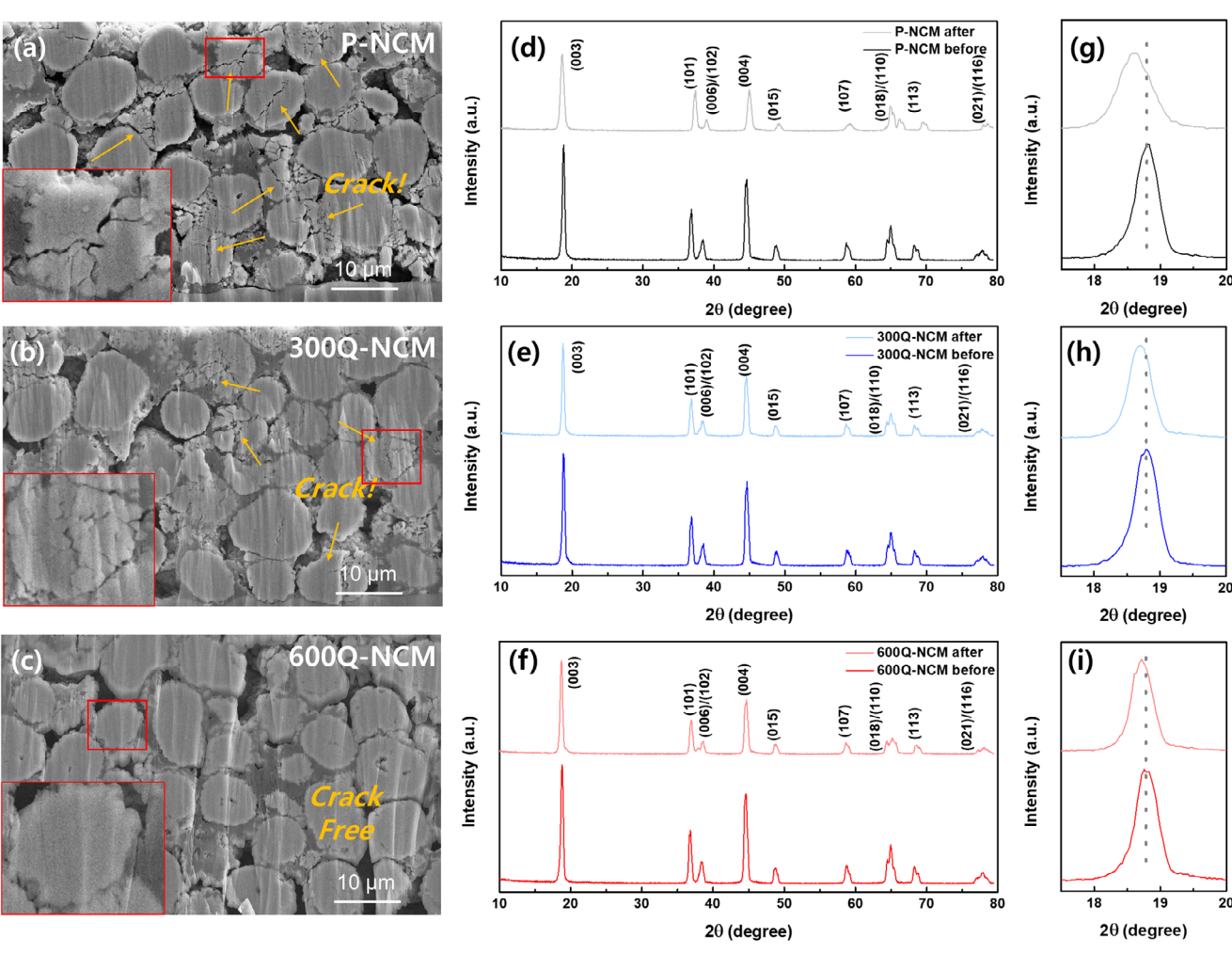


Figure 7. a-c) Cross-sectional SEM images, d-f) XRD results, and g-i) enlarged (003) peak region of P-NCM, 300Q-NCM, and 600Q-NCM after 100 cycles, respectively.

metal dissolution (Figure S16, Supporting Information). Predictably, the highest degree of transition-metal dissolution was measured in P-NCM, while the lowest degree was measured in 600Q-NCM. This indicated that microcrack formation could be effectively suppressed by introducing LiF on both the secondary particles and the interfaces between the primary particles, and its superior structural stability effectively suppressed transition-metal-ion crosstalk.[47] In addition, the enhanced structural stability of 600Q-NCM observed after cycling was further validated by XRD analysis (Figure 7d-i). The downshift of the (003) peak indexed at $\approx 18^{\circ}$ (2 θ degree) reflected a c-axis expansion of the NCM cathode materials, due to repeated volume changes during lithium intercalation/de-intercalation.[48-50] Among the three samples, 600Q-NCM exhibited the smallest peak shift, further confirming that it maintained the most stable structure owing to the protection of both secondary and primary particles. Consequently, we believe that the main roles of the LiF layer at the interfaces between primary particles were mainly to mitigate microcrack formation induced by stress accumulation at interfaces, as well as to suppress electrolyte decomposition at the interfaces between primary particles.

3. Conclusion

Using a simple quenching process with a fluorinated ketone solvent, we designed a single-step surface modification strategy capable of converting residual lithium compounds into a LiF protective layer on both the surface of secondary particles and the interfaces between the primary particles of a high-Ni NCM cathode. 300Q-NCM, which featured a LiF protective layer only on the surface of secondary particles, demonstrated an enhanced cycling performance compared to that of P-NCM. More importantly, 600Q-NCM, which had LiF protective layers on both the surface of the secondary particles and the interfaces between primary particles, exhibited outstanding electrochemical performance, including excellent cycling stability and rate capability, even under severe operating conditions such as high temperatures and high cut-off voltages. dQ/dV and post-mortem analyses revealed that the outstanding electrochemical performance of 600Q-NCM was strongly correlated with the structural stability of the primary and secondary particles. 300Q-NCM prevented electrolyte decomposition on the surfaces of secondary particles owing to the formation of LiF on their surfaces. However, the www.advancedsciencenews.com

_____5111U11

www.small-journal.com

absence of a LiF layer at the interfaces between the primary particles led to continuous microcrack formation, ultimately causing structural collapse of the cathode material during prolonged cycling. In contrast, 600Q-NCM with LiF layers on both the surface of secondary particles and the interfaces between primary particles effectively prevented electrolyte decomposition on the surface of the secondary particles and mitigated microcrack formation induced by stress accumulation at the interfaces, thereby retaining its structural integrity even after prolonged cycling. Consequently, our findings reveal the critical role of the LiF formed at the interfaces between the primary particles in improving the structural stability of high-Ni NCM cathodes. In addition, we believe that our single-step surface modification strategy provides a simple and scalable method for the synthesis of high-Ni NCM cathode materials to achieve long-lasting LIBs.

Supporting Information

Supporting Information is available from the Wiley Online Library or from the author.

Acknowledgements

S.J.P., H.L., and H.-B.L. contributed equally to this work. The authors thank Haifeng Gao, Jiyoung Park, Zhao Liu, Brandon B. Van Leer, Peter Priecel, and Bartlomiej Winiarski (Thermo Fisher Scientific) for their help with using the FIB-TOFSIMS system and Dr. Hyeon-Ah Ju for the assistance of additional STEM and EELS analysis. K. J. Kim acknowledges the support of the Basic Science Research Program (RS-2024-00455177) through the National Research Foundation of Korea (NRF) funded by the Ministry of Science, ICT. Y.-M.K. acknowledges the support of the National Research Foundation of Korea (NRF) grant (RS-2023-NR076943) funded by the Korean government in Korea.

Conflict of Interest

The authors declare no conflict of interest.

Data Availability Statement

The data that support the findings of this study are available from the corresponding author upon reasonable request.

Keywords

artificial LiF-rich CEI layer, fluorinated ketone, Ni-rich layered cathode, primary-particle coating, quenching

Received: June 17, 2025 Revised: August 12, 2025 Published online: September 4, 2025

- T. Yang, K. Zhang, Y. Zuo, J. Song, Y. Yang, C. Gao, T. Chen, H. Wang, W. Xiao, Z. Jiang, D. Xia, Nat. Sustain. 2024, 7, 1204.
- [2] T. Liu, L. Yu, J. Liu, A. Dai, T. Zhou, J. Wang, W. Huang, L. Li, M. Li, T. Li, X. Huang, X. Xiao, M. Ge, L. Ma, Z. Zhuo, R. Amine, Y. S. Chu, W. K. Lee, J. Wen, K. Amine, *Nat. Energy* **2024**, *9*, 1252.

- [3] Y. Sun, J. Ma, D. Wu, C. Wang, Y. Zhao, M. Zheng, R. Yu, W. Li, M. Li, Y. Gao, X. Lin, H. Duan, J. Fu, Z. Wang, R. Li, M. D. Gu, T. K. Sham, X. Sun, *Energy Environ. Sci.* 2024, 17, 5124.
- [4] Z. Li, Y. Wang, J. Wang, C. Wu, W. Wang, Y. Chen, C. Hu, K. Mo, T. Gao, Y. S. He, Z. Ren, Y. Zhang, X. Liu, N. Liu, L. Chen, K. Wu, C. Shen, Z. F. Ma, L. Li, *Nat. Commun.* 2024, 15, 10216.
- [5] J. Guo, P. Li, F. Piccolo, Y. Jie, H. Jia, R. Cao, S. Jiao, P. Adelhelm, Y. Xu, ACS Energy Lett. 2025, 10, 2318.
- [6] Z. Wu, C. Zhang, F. Yuan, M. Lyu, P. Yang, L. Zhang, M. Zhou, L. Wang, S. Zhang, L. Wang, Nano Energy 2024, 126, 109620.
- [7] B. Aktekin, A. E. Sedykh, K. Müller-Buschbaum, A. Henss, J. Janek, Adv. Funct. Mater. 2024, 34, 2313252.
- [8] W. M. Seong, K. H. Cho, J. W. Park, H. Park, D. Eum, M. H. Lee, I. seok, S. Kim, J. Lim, K. Kang, Angew. Chemie. Int. Ed. 2020, 59, 18662.
- [9] M. Jiang, D. L. Danilov, R. A. Eichel, P. H. L. Notten, Adv. Energy Mater. 2021, 11, 2103005.
- [10] S. Oswald, R. Wilhelm, T. Kratky, L. Szentmiklósi, B. Maróti, I. Harsányi, S. A. Hallweger, G. Kieslich, S. Günther, H. A. Gasteiger, J. Mater. Chem. A 2024, 12, 25140.
- [11] D. Pritzl, T. Teufl, A. T. S. Freiberg, B. Strehle, J. Sicklinger, H. Sommer, P. Hartmann, H. A. Gasteiger, J. Electrochem. Soc. 2019, 166, A4056.
- [12] X. Huang, J. Duan, J. He, H. Shi, Y. Li, Y. Zhang, D. Wang, P. Dong, Mater. Today Energy 2020, 17, 100440.
- [13] W. Lee, S. Lee, E. Lee, M. Choi, R. Thangavel, Y. Lee, W. S. Yoon, *Energy Storage Mater.* 2022, 44, 441.
- [14] Y. Li, H. Shi, J. He, X. Li, Z. Chen, Y. Zhang, L. Deng, P. Dong, D. Wang, Y. Zhang, J. Duan, Appl. Surf. Sci. 2022, 593, 153409.
- [15] Y. H. Du, H. Sheng, X. H. Meng, X. D. Zhang, Y. G. Zou, J. Y. Liang, M. Fan, F. Wang, J. Tang, F. F. Cao, J. L. Shi, X. F. Cao, Y. G. Guo, *Nano Energy* 2022, 94, 106901.
- [16] T. Sattar, S. J. Sim, B. S. Jin, H. S. Kim, Sci. Rep. 2021, 11, 18590.
- [17] W. Wang, L. Wu, Z. Li, K. Huang, J. Jiang, Z. Chen, X. Qi, H. Dou, X. Zhang, ACS Appl. Energy Mater. 2020, 3, 12423.
- [18] J. Li, J. Xiang, G. Yi, Y. Tang, H. Shao, X. Liu, B. Shan, R. Chen, *Coatings* 2022, 12, 84.
- [19] S. Zhang, J. Wu, N. Jiang, H. Sun, H. Yang, L. Shen, M. Zhou, W. Liu, H. Zhou, H. Zhao, Adv. Energy Mater. 2024, 14, 2401123.
- [20] T. Liu, J. Ma, T. He, R. Meng, L. Chen, S. Meng, K. Liao, H. Lu, J. Ma, C. Zhang, J. Yang, Energy Storage Mater. 2024, 71, 103577.
- [21] G. Yang, B. Liu, F. Lai, K. Xue, X. Zhang, H. Wang, M. Xie, C. Wang, Nano Energy 2025, 140, 111009.
- [22] Y. B. Sim, H. Lee, J. Mun, K. J. Kim, J. Energy Chem. 2024, 96, 185.
- [23] S. Huang, T. Xu, Y. Peng, Q. Xu, J. Power Sources 2025, 644,
- [24] K. Liu, Q. Zhang, S. Dai, W. Li, X. Liu, F. Ding, J. Zhang, ACS Appl. Mater. Interfaces 2018, 10, 34153.
- [25] X. Xiong, Z. Wang, X. Yin, H. Guo, X. Li, Mater. Lett. 2013, 110, 4.
- [26] J. Park, Y. Kim, Y. Kim, J. Park, D. G. Lee, Y. Lee, J. Hwang, K. Y. Park, D. Lee, Chem. Eng. J. 2023, 467, 143335.
- [27] K. Wang, Q. Mao, X. Lu, J. Zhang, H. Huang, Y. Gan, X. He, X. Xia, W. Zhang, Y. Xia, Sustain. Mater. Technol. 2023, 38, 00713.
- [28] P. S. Llanos, Z. Ahaliabadeh, V. Miikkulainen, J. Lahtinen, L. Yao, H. Jiang, T. Kankaanpää, T. M. Kallio, ACS Appl. Mater. Interfaces 2024, 16, 2216.
- [29] K. Wei, J. Li, W. Huang, L. Wang, Solid State Ionics **2024**, 405, 116436.
- [30] A. Štefančič, C. A. F. Vaz, D. Baster, E. Müller, M. El Kazzi, Chem-SusChem 2025, 18, 202402057.
- [31] H. B. Lee, M. H. Jung, Y. H. Kim, E. B. Park, W. S. Jang, S. J. Kim, K. ju Choi, J. young Park, K. bum Hwang, J. H. Shim, S. Yoon, Y. M. Kim, J. Anal. Sci. Technol. 2023, 14, 47.
- [32] G. T. Park, H. H. Ryu, T. C. Noh, G. C. Kang, Y. K. Sun, Mater. Today 2022, 52, 9.
- [33] Y. hong Luo, Q. lin Pan, H. xin Wei, Y. de Huang, L. bo Tang, Z. yu Wang, Z. jiang He, C. Yan, J. Mao, K. hua Dai, X. hui Zhang, J. chao Zheng, Nano Energy 2022, 102, 107626.

www.advancedsciencenews.com



- [34] S. J. Park, Y. J. Choi, J. Cheon, H. Kim, J. W. Lee, T. Yim, K. J. Kim, K. J. Kim, J. Mater. Chem. A 2024, 12, 11551.
- [35] W. Lv, C. Zhu, J. Chen, C. Ou, Q. Zhang, S. Zhong, Chem. Eng. J. 2021, 418, 129400.
- [36] T. Sui, B. Song, J. Dluhos, L. Lu, A. M. Korsunsky, Nano Energy 2015, 17, 254.
- [37] A. Priebe, J. Michler, Materials 2023, 16, 2090.
- [38] J. L. S. Lee, I. S. Gilmore, M. P. Seah, A. P. Levick, A. G. Shard, Surf. Interface Anal. 2012, 44, 238.
- [39] J. Li, Y. Zhang, X. Chen, L. Lu, H. Liu, F. Gao, S. An, X. Wang, X. Qiu, J. Electrochem. Soc. 2024, 171, 050528.
- [40] X. Zhang, E. Fan, J. Lin, Y. Zhao, Q. Huang, S. Ma, R. Chen, F. Wu, L. Li, Energy Storage Mater. 2025, 74, 103914.
- [41] Z. Qin, Y. Zhang, W. Luo, T. Zhang, T. Wang, L. Ni, H. Wang, N. Zhang, X. Liu, J. Zhou, G. Chen, Angew. Chemie Int. Ed. 2023, 62, 202218672.
- [42] L. Qiu, M. Zhang, Y. Song, Z. Wu, Y. F. Zhu, J. Zhang, D. Wang, H. Y. Hu, H. W. Li, H. R. Liu, X. B. Jia, J. Peng, S. Chen, Z. Yang, Y. Xiao, X. Guo, Carbon Energy 2023, 5, 298.

- [43] L. Chen, C. Xing, Z. Yang, S. Tao, Y. Zhang, G. Wang, P. Yang, J. Song, J. Chen, L. Fei, Adv. Funct. Mater. 2024, 35, 2411182.
- [44] C. Li, X. Zhang, Z. Yang, H. Lv, T. Song, S. Lu, Y. Zhang, T. Yang, F. Xu, F. Wu, D. Mu, J. Energy Chem. 2023, 87, 342.
- [45] S. Liu, J. Su, J. Zhao, X. Chen, C. Zhang, T. Huang, J. Wu, A. Yu, J. Power Sources 2018, 393, 92.
- [46] T. Zhu, G. Wang, J. Hou, W. Sun, C. Song, Q. Yuan, C. Zhang, X. Lei, Y. Su, M. Chen, Y. Song, J. Zhao, Adv. Funct. Mater. 2025, 35, 2501870.
- [47] Y. Min Kim, J. In Choi, B. Keun Park, J. Woo Han, J. W. Lee, H. seung Kim, K. Jae Kim, Chem. Eng. J. 2024, 486, 150354.
- [48] F. Friedrich, B. Strehle, A. T. S. Freiberg, K. Kleiner, S. J. Day, C. Erk, M. Piana, H. A. Gasteiger, J. Electrochem. Soc. 2019, 166, A3760.
- [49] W. Li, X. Liu, Q. Xie, Y. You, M. Chi, A. Manthiram, Chem. Mater. 2020, 32, 7796.
- [50] L. De Biasi, A. O. Kondrakov, H. Geßwein, T. Brezesinski, P. Hartmann, J. Janek, J. Phys. Chem. C 2017, 121, 26163.